

Frequency-modulated impulse response photothermal detection through optical reflectance. 1: Theory

Andreas Mandelis and Joan F. Power

The 3-D theory of impulse response photothermal detection in opaque (i.e., photothermally saturated) solids through the dependence of the surface temperature optical reflectance on the mathematical equivalent of an optical impulse (the Green's function) is presented. The theory is extended to include the effects of the finite spatial extent of the photothermal laser source. Explicit expressions for the time-dependent temperature field have been obtained in the experimentally important cases of semi-infinite solids and solids of finite thickness in contact with thermally insulating or conducting backings.

I. Introduction

The optical generation of thermal wave phenomena in materials has in recent years provided a powerful method of microscopy for the nondestructive evaluation of integrated circuits and other device materials. The unique advantage posed by thermal wave microscopy is its ability to perform nondestructive thermal depth profiling of extremely shallow surface layers in materials. The short-range critically damped character of thermal waves in solid media and the decrease in thermal penetration depth with increased modulation frequency are responsible for these high resolution depth profiling capabilities. The use of focused lasers to generate highly localized heating at the surface of a material has enabled the resolution of micron sized features.

Recently, a very powerful methodology, in which thermal wave phenomena could be detected noninvasively via optically induced thermoelastic deformations^{1,2} and optical reflectivity changes³ at the sample surface, has emerged. Detection was achieved via a pump-probe configuration in which a highly focused heating beam was absorbed at the sample surface, inducing a thermal bump due to the thermoelastic effect, with simultaneous changes in sample reflectance

due to variations of the surface temperature. Detection of thermal waves was achieved both thermoelastically, in which the thermal surface deformations produced deflections of the probe beam, or by changes in the sample's surface reflectance with temperature, which produced variations in the integrated intensity of the probe beam. Because of the availability of fast photodiodes and quad-cell detectors, the very wide bandwidth of the technique is, therefore, capable of resolving thermal images limited by optical rather than thermal diffraction.

Previous work which has used this technique for thermal imaging has been carried out exclusively in the frequency domain, in which the modulation frequency of the irradiation source was varied on a point-by-point basis, and the reflectivity or thermoelastic response signals were detected narrowband using a lock-in amplifier. Recently, Eesley *et al.*⁴⁻⁶ have introduced pulsed laser picosecond transient thermoreflectance (TTR) as a fast sensitive technique capable of measuring thin film thermal diffusivity and time-resolved thermal transport processes in metal samples. This technique is also based on the principle of optical reflectivity changes at the sample surface as a result of local laser heating. Time-domain pulsed-laser schemes have further been used with other photothermal wave imaging systems such as the flash radiometric technique developed by Leung and Tam,⁷ which is based on the noncontact detection of transient infrared (blackbody) radiation from a sample heated by a short optical pulse. These schemes, however successful with materials tolerant to steep temperature excursions, cannot be used with delicate materials, such as semiconductor substrates and devices, without severe restrictions in the exciting laser beam parameters, as the high pump irradiances tend to alter (anneal or otherwise damage) the surfaces and device structures

When this work was done both authors were with University of Toronto, Department of Mechanical Engineering, Photoacoustic & Photothermal Sciences Laboratory, Toronto, Ontario M5S 1A5, Canada; Joan Power is now with McGill University, Chemistry Department.

Received 1 December 1987.

0003-6935/88/163397-11\$02.00/0.

© 1988 Optical Society of America.

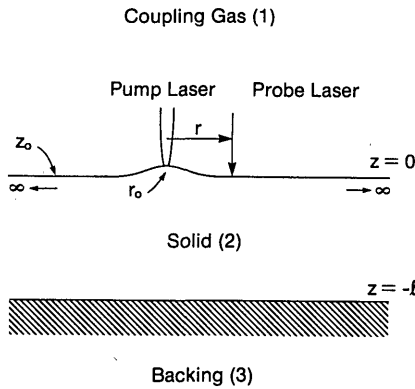


Fig. 1. Three-dimensional geometry for impulse response (Green's function) heat conduction generation due to an (effective) laser pulse; $R^2 = r^2 + (z - z_0)^2$, where the exciting source is assumed to be at the sample surface ($z_0 = 0$).

with which the beam interacts.⁸ Furthermore, it has been shown that the greatest care must be exercised when using photothermal radiometry with some categories of samples, because the heat source is often difficult to define due to the weak IR emissivity of the sample.⁹

As an alternative to pulsed laser excitation, we recently introduced fast impulse-response photothermal wave excitation and detection techniques, which, when coupled with photothermal instrumentation of wide-band frequency response, avoid the destructive shortcomings of pulsed laser excitation while retaining desirable time-resolved advantages.^{10,11} Impulse response measurements are effected by Fourier transformation and spectral analysis of photothermal signals, which give the mathematical equivalent of a pulsed pump laser beam, except that input irradiances are orders of magnitude lower than those of pulsed lasers, with a concomitant large increase in sample optical damage threshold.

The main advantage of measurements of photothermal impulse responses, compared to single-frequency beam intensity modulation methods, is the simplicity of interpretation of such measurements which yield a direct visualization of an impulse source of thermal energy diffusing toward or away from the sample surface in time. Signal components due to the arrival at the surface of energy reflected off boundaries defined by buried layers in the material contain photothermal image information, which is now dispersed over a time coordinate rather than over modulation frequency. The obvious relationship between vertical depth of a buried thermal feature and the transit time of thermal energy to the sample surface are responsible for the time dispersion of photothermal image information.

Impulse response analysis of photothermal signals can be handled by Green's function formalisms of transient heat conduction.^{10,11} In this work, we present a generalized 3-D thermal wave theory which provides analytical time-domain expressions for the Green's function evolution in homogeneous solids and thin surface layers at, or close to, the sample surface. This 3-D theory is expected to be generally useful both in

quantitative thermal characterization and imaging applications with well-defined geometries and is directly applicable to the wide bandwidth optical reflectance thermal wave measurement methodology reported in Part 2.

II. General Theory of 3-D Photothermal Green's Function in Solids

The present model is concerned with a prediction of the form of the Green's function for thermal diffusion at a solid surface due to an impulsive heat source. The origin of the heat source is considered to be thermal energy generation following absorption of an optical impulse, which is the mathematical equivalent to random or FM excitation with a chirped wavetrain on the surface. In our experimental configuration, thermal wave information is recovered from the temperature dependence of the surface reflectivity as predicted by the reflectivity response.¹²

$$\Delta R(r, z = 0, t) = R_0 + \left(\frac{\partial R}{\partial T} \right)_{T=T_0} T_2(r, z = 0, t), \quad (1)$$

where R_0 is the surface reflectivity of the sample at ambient temperature T_0 , $(\partial R)/(\partial T)$ is the temperature coefficient of surface reflectance, assumed to be constant over the interval of temperature changes studied, T_2 is the time-dependent temperature variation in the material due to thermal wave propagation. The optical reflectivity signal is a direct probe of the thermal wave phenomena because of the direct proportionality between ΔR measured at the detector and the surface temperature variation T_2 . (In contrast, the thermoelastic deformation signal is proportional to the temperature gradient, $\partial T/\partial r$, providing a more indirect thermal probe.) The solution of the relevant coupled heat conduction equations to obtain $T_2(r, z = 0, t)$ will, therefore, yield the form of the observed reflectivity response directly.

The geometry adopted for the purposes of this work is shown in Fig. 1. The sample solid (2) is assumed to be of infinite lateral extent, a valid approximation in view of the very tightly focused laser pump and probe beams ($\sim 3 \mu\text{m}$) in our experiments. The temperature distribution $T_2(r, z, t)$ can be obtained from the solution in cylindrical coordinates of homogeneous heat conduction equations of the form

$$\nabla^2 T_i(r, z, t) - \frac{1}{\alpha_i} \frac{\partial T_i}{\partial t}(r, z, t) = 0, \quad (2)$$

$i = (1)$ gas, (2) solid, or (3) backing, subject to homogeneous boundary conditions with an impulsive contribution (a Dirac δ -function in time) due to the cylindrical thermal source at $z = 0$. In Eq. (2), α_i is the thermal diffusivity of region i . Taking Laplace transforms ($t \rightarrow s$) of Eq. (2) subject to the initial conditions,

$$T_i(r, z, 0) = 0 \quad (3)$$

yields

$$\nabla^2 \bar{T}_i(r, z, s) - q_i^2 \bar{T}_i(r, z, s) = 0, \quad (4)$$

where

$$q_i(s) \equiv (s/\alpha_i)^{1/2}. \quad (5)$$

The system of Eqs. (4) can be solved using the conventional boundary conditions of temperature and heat flux continuity at the (1,2) and (2,3) interfaces.¹³ There exists a formal correspondence between the frequency-domain harmonic optical excitation and photothermal response of a solid using Fourier analysis as described by Chow¹³ and the present time-resolved impulse response treatment which employs Laplace transform analysis. This correspondence manifests itself in the physically equivalent phenomena of response phase lag (frequency-domain) and time delay (time-domain) as discussed elsewhere.¹⁴ With these

$$A - C - D = E, \quad (11a)$$

$$B - C \exp(-\sigma_2 l) - D \exp(\sigma_2 l) = E \exp(-\sigma_2 l), \quad (11b)$$

$$-k_1 \sigma_1 A - k_2 \sigma_2 C + k_2 \sigma_2 D = -k_2 \sigma_2 E, \quad (11c)$$

$$k_3 \sigma_3 B - k_2 \sigma_2 C \exp(-\sigma_2 l) + k_2 \sigma_2 D \exp(\sigma_2 l) = -k_2 \sigma_2 E \exp(-\sigma_2 l), \quad (11d)$$

where

$$E \equiv \frac{k}{4\pi\alpha_2\sigma_2}. \quad (12)$$

Solving for $A(k)$ in a straightforward fashion gives

$$A(k) = \frac{k(1 + b_{32})[\exp(\sigma_2 l) + \exp(-\sigma_2 l)]}{2\pi\alpha_2\sigma_2[(1 + b_{32})(1 + b_{12}) \exp(\sigma_2 l) - (1 - b_{32})(1 - b_{12}) \exp(-\sigma_2 l)]}, \quad (13)$$

remarks the Laplace transforms of the boundary conditions can be written

$$\bar{T}_1(r, 0, s) = \bar{T}_2(r, 0, s) \quad (6a)$$

$$\bar{T}_2(r, -l, s) = \bar{T}_3(r, -l, s), \quad (6b)$$

$$k_1 \frac{\partial \bar{T}_1}{\partial z}(r, 0, s) = k_2 \frac{\partial \bar{T}_2}{\partial z}(r, 0, s), \quad (6c)$$

$$k_2 \frac{\partial \bar{T}_2}{\partial z}(r, -l, s) = k_3 \frac{\partial \bar{T}_3}{\partial z}(r, -l, s), \quad (6d)$$

where k_i is the thermal conductivity of the i th region. Solutions to Eqs. (4) can be written using Sommerfeld's method as applied by Stratton.¹⁵

$$\bar{T}_1(r, z, s) = \int_0^\infty J_0(kr) A(k) \exp(-\sigma_1 z) dk; \quad z \geq 0, \quad (7)$$

$$\bar{T}_2(r, z, s) = \int_0^\infty J_0(kr) \left[C(k) \exp(\sigma_2 z) + D(k) \exp(-\sigma_2 z) + \frac{k \exp(-\sigma_2 |z|)}{4\pi\alpha_2\sigma_2} \right] dk; \quad 0 \geq z \geq -l, \quad (8)$$

$$\bar{T}_3(r, z, s) = \int_0^\infty B(k) J_0(kr) \exp[\sigma_3(z + l)] dk; \quad z \leq -l, \quad (9)$$

where A, B, C, D are constants to be determined by the boundary conditions.

The last term in brackets of the integrand in Eq. (8) is due to the instantaneous source at $z_0 = 0$ in the $z \leq 0$ half-space (Fig. 1). In Eqs. (7)–(9), we have defined

$$\sigma_i(s) \equiv [k^2 + q_i^2(s)]^{1/2}, \quad (10)$$

and J_0 is the Bessel function of zeroth order. Here it appears due to the cylindrical geometry imposed by the symmetry of the laser beams. Now we only need solve for the Laplace transform of the temperature field at the gas–solid interface, $\bar{T}_1(r, 0, s)$, where probing of the temperature dependence of the reflectivity takes place. Therefore, substituting Eqs. (7)–(9) into Eqs. (6) gives the following algebraic equations for A, B, C, D :

with

$$b_{ij}(s) \equiv k_i \sigma_i(s) / k_j \sigma_j(s). \quad (14)$$

Now, rearranging the denominator of Eq. (13) and using the expansion

$$(1 - x)^{-1} = \sum_{n=0}^{\infty} x^n; \quad x < 1 \quad (15)$$

transforms $A(k)$ to

$$A(k) = \frac{k[1 + \exp(-2\sigma_2 l)]}{2\pi\alpha_2\sigma_2(1 + b_{12})} \sum_{n=0}^{\infty} \zeta^n \exp(-2n\sigma_2 l), \quad (16)$$

where

$$\zeta \equiv \frac{(1 - b_{32})(1 - b_{12})}{(1 + b_{32})(1 + b_{12})}. \quad (17)$$

Because of the low thermal conductivity of gases relative to solid materials in general, the condition

$$k_2 \gg k_1 \quad (18)$$

will be assumed to hold for all cases of experimental interest. In this condition

$$\zeta \approx \frac{1 - b_{32}}{1 + b_{32}} \quad (19)$$

so that substitution of Eq. (16) into the expression for the Laplace transform of the gas temperature $\bar{T}_1(r, z, s)$, Eq. (7) yields

$$\bar{T}_1(r, z, s) = \frac{1}{2\pi\alpha_2} \int_0^\infty \left[\frac{1 + \exp(-2\sigma_2 l)}{\sigma_2} \right] \sum_{n=0}^{\infty} \zeta^n \times \exp(-2n\sigma_2 l - \sigma_1 z) J_0(kr) k dk \quad z \geq 0 \quad (20)$$

On separating out the $n = 0$ term in Eq. (20) we can write

$$\begin{aligned} \bar{T}_1(r,z,s) = & \frac{1}{2\pi\alpha_2} \left\{ \int_0^\infty \frac{\exp(-\sigma_1 z)}{\sigma_2} J_0(kr) k dk \right. \\ & + \int_0^\infty \frac{\exp(-2\sigma_2 l - \sigma_1 z)}{\sigma_2} J_0(kr) k dk \\ & + \sum_{n=1}^\infty \int_0^\infty \left(\frac{\sigma_1^n}{\sigma_2} \right) \exp(-2n\sigma_2 l - \sigma_1 z) J_0(kr) k dk \\ & + \sum_{n=1}^\infty \int_0^\infty \left(\frac{\sigma_1^n}{\sigma_2} \right) \\ & \left. \times \exp[-2(n+1)\sigma_2 l - \sigma_1 z] J_0(kr) k dk \right\}. \quad (21) \end{aligned}$$

It is worthwhile noticing that the last three terms in Eq. (21) appear due to the presence of a finite solid boundary at $z = -l$. In the limit $l \rightarrow \infty$, the first term represents the thermal response in the gas due to a semi-infinite solid excited by a unit cylindrical thermal impulse of infinitesimal spatial extent in both r and z dimensions at $t = 0$.

Equation (21), which forms the basis for our 3-D point irradiation model, is a zero-order Hankel transform. It expresses the solution to the three-layer problem gas-solid backing in the Laplace domain as an integral function over the Bessel wavenumber k . It is of interest to point out that Eq. (20) can be written equivalently in the Hankel transform form

$$\bar{T}_1(r,z,s) = \frac{1}{2\pi\alpha_2} \int_0^\infty F(z,s;k) J_0(kr) k dk, \quad (22)$$

where the kernel $F(z,s;k)$ becomes equivalent to the Laplace transform of the 1-D problem (uniform irradiation along the r direction)¹⁴ in the limit of $k = 0$. In that limit, the net effect on $F(z,s;0)$ is that the variables $\sigma_i(s)$ are replaced by the respective $q_i(s)$. This feature has also been pointed out by Rosencwaig and Opsal in a frequency-domain derivation of the expression for the surface temperature of a multilayered sample via thermoacoustic detection,¹⁶ and once again it reflects the formal equivalence between time and frequency-domain formalisms.

Analytical inversions of Eq. (21) are possible, albeit fairly complicated, in the general case. For our purposes, simplified analytical inversions will be obtained for the relevant experimentally realistic case limits of interest.

III. Special Cases

A. Semi-Infinite Solid

To a first approximation, the limit of a semi-infinite solid ($l \rightarrow \infty$) will be considered. In this condition we obtain

$$\bar{T}_1(r,z,s) = \frac{1}{2\pi\alpha_2} \int_0^\infty \frac{\exp(-z\sqrt{k^2 + q_1^2})}{\sqrt{k^2 + q_2^2}} J_0(kr) k dk. \quad (23)$$

For the experimentally important case where the temperature field is required at the probe laser point on the sample surface, $z = 0$, and Eq. (23) becomes

$$\bar{T}_1(r,0,s) = \frac{1}{2\pi\alpha_2} \int_0^\infty \frac{J_0(kr) k dk}{\sqrt{k^2 + q_2^2}}. \quad (24)$$

This integral can be solved by use of a method presented by Bellman *et al.*¹⁷ and outlined in a modified form in Appendix A, as applied to this particular integral. Equations (24) and (A5) give

$$T_1(r,0,t) = \frac{1}{4(\pi\alpha_2 t)^{3/2}} \exp(-r^2/4\alpha_2 t). \quad (25)$$

Equation (25) is the Green's function showing the explicit spatial and temporal dependence of the surface temperature of a semi-infinite 3-D solid, following an impulsive excitation by a point source at $r_0 = z_0 = 0$. The form (25) is valid for all locations r on the surface in relation to the time-dependent thermal diffusion length¹⁴

$$\mu_s(t) \equiv 2\sqrt{\alpha_2 t} \quad (26)$$

and is in agreement with other derivations of the Green's function predicted for the same semi-infinite geometry, the presence of the interface at $z = 0$ contributing twice the value of the Green's function for infinite geometry.¹⁸

B. Solid of Finite Thickness on a Thermally Insulating Backing ($b_{32} \ll 1$)

In this condition, $\zeta \approx 1$, and Eq. (21) becomes

$$\begin{aligned} \bar{T}_1(r,0,s) = & \frac{1}{2\pi\alpha_2} \left\{ \int_0^\infty \frac{1}{\sigma_2} J_0(kr) k dk + \int_0^\infty \frac{\exp(-2\sigma_2 l)}{\sigma_2} J_0(kr) k dk \right. \\ & + \sum_{n=1}^\infty \int_0^\infty \frac{\exp(-2n\sigma_2 l)}{\sigma_2} J_0(kr) k dk \\ & \left. + \sum_{n=1}^\infty \int_0^\infty \frac{\exp[-2(n+1)\sigma_2 l]}{\sigma_1} J_0(kr) k dk \right\}. \quad (27) \end{aligned}$$

Each integral in Eq. (27) can be solved according to the general method outlined in Appendix B. The temperature profile at the solid surface thus becomes

$$\begin{aligned} T_1(r,0,t) = & \frac{\exp(-r^2/4\alpha_2 t)}{4(\pi\alpha_2 t)^{3/2}} \\ & \times \sum_{n=0}^\infty (\exp[-(2n)l^2/4\alpha_2 t] + \exp[-[2(n+1)l]^2/4\alpha_2 t]). \quad (28) \end{aligned}$$

This form of the surface temperature profile impulse response can be shown to be the $z = 0$ limit of the bulk solid temperature profile obtained for double adiabatic boundaries, as follows. Instead of placing a heat source in the sample layer formally, it is possible to solve the physically equivalent problem of the solid of Fig. 1, in which an instantaneous 3-D point-source heat flux is present at the $z = 0$ boundary at $t = 0$. Using the homogeneous part of Eq. (8) for the solid temperature,

$$\bar{T}_2^H(r,z,s) = \int_0^\infty J_0(kr) [C(k) \exp(\sigma_2 z) + D(k) \exp(-\sigma_2 z)] dk \quad (29)$$

with the boundary heat flux condition

$$\frac{\partial T_2}{\partial z}(r,0,t) = \frac{1}{4\pi r} \delta(r)\delta(t). \quad (30)$$

The Hankel transform of the boundary condition is

$$\frac{\partial \bar{T}_2^H}{\partial z}(k,0,t) = 2\pi\delta(t) \int_0^\infty \frac{J_0(kr)\delta(r)}{4\pi r} r dr = \frac{1}{2}\delta(t), \quad (31)$$

Eq. (31) has the Laplace transform

$$\frac{\partial \bar{T}_2^H}{\partial z}(k,0,s) = \frac{1}{2}, \quad (32)$$

so that

$$\frac{\partial \bar{T}_2^H}{\partial z}(r,0,s) = \frac{1}{2} \int_0^\infty J_0(kr)k dk. \quad (33)$$

The second boundary condition is the adiabatic condition ($b_{32} \ll 1$) at $z = -l$:

$$\frac{\partial \bar{T}_2^H}{\partial z}(r,-l,s) = 0. \quad (34)$$

From Eqs. (29), (33), and (34) one obtains algebraic relations for the integrands

$$\sigma_2[C(k) - D(k)] = \frac{k}{2}, \quad (35a)$$

$$C(k) \exp(-\sigma_2 l) = D(k) \exp(\sigma_2 l), \quad (35b)$$

so that

$$C(k) = \frac{k}{2\sigma_2} \left[\frac{1}{1 - \exp(-2\sigma_2 l)} \right], \quad (36)$$

$$D(k) = \frac{k}{2\sigma_2} \left[\frac{\exp(-2\sigma_2 l)}{1 - \exp(-2\sigma_2 l)} \right]. \quad (37)$$

Expanding the denominators, substituting into Eq. (29), and Hankel transforming by use of Appendix B give the expression for the solid's temperature field in response to an impulsive excitation at $z = 0$:

$$T_2(r,z,t) = \frac{\exp(-r^2/4\alpha_2 t)}{4(\pi\alpha_2 t)^{3/2}} \sum_{n=0}^{\infty} \{ \exp[-(2nl - z)^2/4\alpha_2 t] + \exp[-[2(n+1)l + z]^2/4\alpha_2 t] \} \quad 0 \geq z \geq -l. \quad (38)$$

$$\begin{aligned} T_1^d(r,0,t) &= \int_0^\infty \int_{-l}^0 \int_0^{2\pi} \int_0^\infty T_1(r,0,t;r_0,0,t_0) Q(r_0,z_0,t_0) r_0 dr_0 dz_0 d\theta_0 dt_0 \\ &= \frac{\beta P_0}{4(\pi\alpha_2)^{3/2}} \int_0^\infty \int_0^\infty \int_0^{2\pi} \frac{\exp[-(r-r_0)^2/4\alpha_2(t-t_0)] \delta(t_0)}{(t-t_0)^{3/2}} \exp(-r_0^2/w_0^2) r_0 dr_0 d\theta_0 dt_0 \int_{-l}^0 \exp(\beta z_0) dz_0 \\ &= \frac{P_0}{4(\pi\alpha_2 t)^{3/2}} \int_0^{2\pi} \int_0^\infty \exp[-(r-r_0)^2/4\alpha_2 t] \exp(-r_0^2/w_0^2) r_0 dr_0 d\theta_0, \end{aligned} \quad (42)$$

It is instructive to point out that Eq. (38) may also be verified to be physically correct by use of a graphic representation of the Method of Images. This will be demonstrated in Sec. V.

C. Solid of Finite Thickness on a Thermally Conducting Backing ($b_{32} \gg 1$)

In this case we are dealing with the physical situation in which a heat sink is attached to the rear surface

of the sample. Now $\zeta = -1$, and Eq. (21) can be written

$$\begin{aligned} \bar{T}_1(r,0,s) &= \frac{1}{2\pi\alpha_2} \left\{ \bar{I}_1(r,0,s) + \bar{I}_{2l}(r,0,s) \right. \\ &\quad + \sum_{n=1}^{\infty} (-1)^n \bar{I}_{2nl}(r,0,s) \\ &\quad \left. + \sum_{n=1}^{\infty} (-1)^n \bar{I}_{2(n+1)l}(r,0,s) \right\}, \end{aligned} \quad (39)$$

where the integrals \bar{I} have been defined in Appendices A and B. Using results from the Appendices, the temperature profile of the sample surface becomes

$$\begin{aligned} T_1(r,0,t) &= \frac{\exp(-r^2/4\alpha_2 t)}{4(\pi\alpha_2 t)^{3/2}} \sum_{n=0}^{\infty} (-1)^n (\exp[-(2nl)^2/4\alpha_2 t] \\ &\quad + \exp[-[2(n+1)l]^2/4\alpha_2 t]). \end{aligned} \quad (40)$$

A similarly structured expression has been previously derived for the simpler case of a 1-D temperature field with an adiabatic boundary condition at $z = 0$ and a perfect heat sink at $z = -l$ (temperature kept at zero)¹⁹ using the Method of Images.

IV. Effects of Spatially Distributed Photothermal Source

Pump laser beam profile effects can be readily incorporated in the Green's function analysis for all three of the cases just considered. The simplest example is the semi-infinite case. However, the treatment developed in this section applies identically to the radial part of the other two cases.

Assuming a radially distributed and temporally impulsive Gaussian beam profile impinging on an optically opaque solid of absorption coefficient β , the heat impulse produced per unit volume is given by

$$Q(r,z,t) \approx \beta P_0 \exp(-r^2/w_0^2) \exp(-\beta|z|)\delta(t), \quad (41)$$

where P_0 is the irradiance of the incident laser beam. For such a distributed thermal source, the temperature of the solid surface (semi-infinite case) can be written in terms of the Green's function, Eq. (25):

where $\beta l \gg 1$ was assumed.

Now in cylindrical coordinates

$$(r - r_0)^2 = r^2 + r_0^2 - 2rr_0 \cos(\theta_0 - \theta), \quad (43)$$

and using the result²⁰

$$\int_0^{2\pi} \exp[-(2rr_0/4\alpha_2 t) \cos(\theta_0 - \theta)] d\theta_0 = I_0 \left(\frac{rr_0}{2\alpha_2 t} \right), \quad (44)$$

where I_0 is the modified Bessel function of zero order, we can write

$$T_1^d(r,0,t) = \frac{P_0 \exp(-r^2/4\alpha_2 t)}{4(\pi\alpha_2 t)^{3/2}} \int_0^\infty \exp(-r_0^2/\Omega_0^2) I_0\left(\frac{rr_0}{4\alpha_2 t}\right) r_0 dr_0, \quad (45)$$

with

$$\frac{1}{\Omega_0^2} = \frac{1}{w_0^2} + \frac{1}{4\alpha_2 t}. \quad (46)$$

Equation (45) can be integrated using Weber's first integral²¹ and give

$$T_1^d(r,0,t) = \frac{P_0 w_0^2}{2\pi(\pi\alpha_2 t)^{1/2}(4\alpha_2 t + w_0^2)} \exp[-r^2/(4\alpha_2 t + w_0^2)]. \quad (47)$$

V. Discussion

A. Photothermal Response of Semi-infinite Solids

The time profile of a two-layer sample's response to a surface heat impulse is governed by the nature of the relative thermal properties of the first and second layers. The simplest case theoretically is to extend the thickness of the first layer to infinity, so that the observed profile is predicted by the semi-infinite response.

The semi-infinite response, Eq. (25), clearly provides no depth profiling information, since no energy reaches the second boundary, which is located at an infinite distance from the surface. However, it is useful for the evaluation of the thermal diffusivity of the solid due to the contribution of the radial factor $\exp(-r^2/4\alpha_2 t)$. For an infinitesimally small probe beam, sampling reflectivity changes at $r = 0, z = 0$, the observed response is of the form $At^{-3/2}$, a monotonically decreasing function of time with no explicit profile dependence on α_2 . By displacing the probe beam to increasing offset positions, however, one obtains a sample response of the form,

$$\frac{A}{t^{3/2}} \exp(-r^2/4\alpha_2 t),$$

which yields an impulse response profile with a well-defined maximum at $\tau_d = r^2/6\alpha_2$ due to the finite time required for the radial transit of thermal energy to the offset position r . The situation is described in Fig. 2, which illustrates the response profiles observed for a semi-infinite sample of an insulating material [$\alpha_2 = 6 \times 10^{-8} \text{ m}^2/\text{s}$, typical of an insulating polymer film, such as polyvinylidene fluoride (PVDF)]. The increase in offset position from $r = 0.1 \mu\text{m}$ to $r = 6 \mu\text{m}$ gives a large variation in the peak delay τ_d and peak width $\Delta\tau_d$ due to the slow diffusion of energy in the insulator. Diffusion also controls the rather steep radial drop in the peak intensity, which decays inversely proportional to r^3 . In samples of sufficiently low thermal diffusivity very small offsets will produce large variations in τ_d , so that measurements of α_2 are readily possible with a well-calibrated offset between pump and probe beams. With high thermal diffusivity samples such as metals, on the other hand, large radial offsets are required to produce appreciable peak delays. The radial drop in

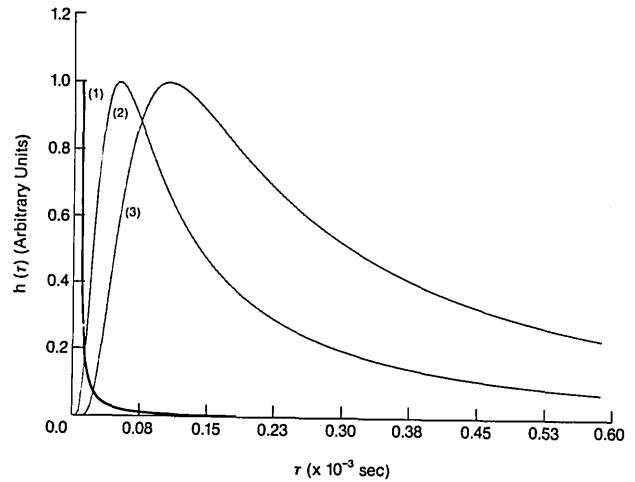


Fig. 2. Impulse response (Green's function) from a 3-D semi-infinite solid sample with thermal diffusivity $\alpha_2 = 6 \times 10^{-8} \text{ m}^2/\text{s}$ (PVDF polymer) using Eq. (25) at pump-probe beam offset distances $r = 0.1 \mu\text{m}$ (1), $4 \mu\text{m}$ (2), and $6 \mu\text{m}$ (3). All curves have been normalized to unity peak value.

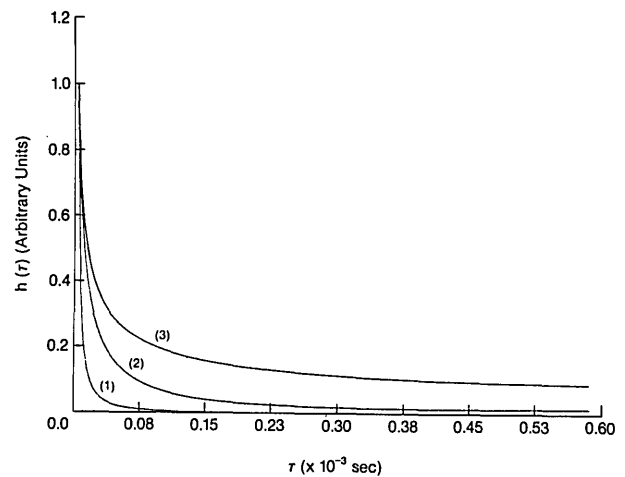


Fig. 3. Impulse response (Green's function) from a 3-D semi-infinite solid sample with $\alpha_2 = 5 \times 10^{-7} \text{ m}^2/\text{s}$ (a glass), including pump beam size effects, Eq. (47), at pump-probe beam offset distance $r = 0.1 \mu\text{m}$. Pump beam waist size $w_0 = 1 \mu\text{m}$ (1), $10 \mu\text{m}$ (2), and 1 mm (3).

signal intensity, however, inhibits detection at large offsets in practice due to an obvious loss of sensitivity.

Another strategy is experimentally available for thermal diffusivity measurements on semi-infinite samples. A transition can be made from the 3-D to the 1-D response by allowing the pump beam radius w_0 to increase to a sufficiently large value. This situation is diagrammed in Fig. 3, which includes the effect of increasing the beam profile dimensions from $w_0 = 1 \times 10^{-6} \text{ m}$ to $w_0 = 1 \times 10^{-3} \text{ m}$ for a semi-infinite sample with $\alpha_2 = 5 \times 10^{-7} \text{ m}^2/\text{s}$ (typical of a glass) according to Eq. (47). The 3-D response with a tightly focused pump beam has the form $At^{-3/2}$ predicted by Eq. (20). At very large pump beam radii, the response approaches the 1-D case $At^{-1/2}$, while intermediate w_0 values produce a time dependence between the 1-D and 3-D

cases. Physically, the controlling behavior is the spatial thermal gradient setup at $t = 0$ in the neighborhood of the point $r = 0$. A tightly focused pump beam produces a large initial transverse gradient at $z = 0$: heat diffuses rapidly away from $r = 0, z = 0$ in three dimensions. As the beam is expanded, the initial transverse thermal gradient in the neighborhood of $r = 0$ drops. For a large enough w_0 , the transverse thermal gradient in the neighborhood of $r = 0$ is effectively zero, so that there is a negligible radial component of transverse heat conduction, and a 1-D decay is observed. A comparison between 1- and 3-D thermal responses is made for the semi-infinite case in Fig. 3.

The 1 \rightarrow 3-D transition in response is predicted analytically from Eq. (47). For small w_0 , we have the condition $w_0^2 \ll 4\alpha_2 t$, and the response is 3-D:

$$T_1^q(r,0,t) \xrightarrow{w_0^2 \ll 4\alpha_2 t} \frac{P_0 w_0^2}{8(\pi\alpha_2 t)^{3/2}} \exp(-r^2/4\alpha_2 t). \quad (48)$$

At the other extreme, when w_0^2 becomes very large, the response approaches the 1-D time dependence resulting from almost uniform surface irradiation with a laser of large beamwaist:

$$T_1^q(r,0,t) \xrightarrow{w_0^2 \gg 4\alpha_2 t} \frac{P_0}{2\pi(\pi\alpha_2 t)^{1/2}} \exp(-r^2/w_0^2). \quad (49)$$

B. Measurements of Thin Layers with Insulated Boundaries

The second special case of interest is the one concerning effectively adiabatic conditions at the boundaries of the sample layer, i.e., at $z = 0$ and $z = -l$. This limiting case of the general theory is experimentally applicable to photothermal measurements on the surface of thermal conductors of unknown thickness or unknown thermal diffusivity, which are in intimate contact with an insulating layer at $z = -l$. An alternative geometry would be that of a freely suspended thin film.

The impulse response of a photothermally saturated sample with adiabatic boundary conditions can be interpreted graphically on consideration of Eq. (38) in the form

$$T_2(r,z,t) = \frac{\exp(-r^2/4\alpha_2 t)}{8(\pi\alpha_2 t)^{3/2}} \left\{ \exp(-z^2/4\alpha_2 t) + \sum_{n=0}^{\infty} (\exp[-(2nl - z)^2/4\alpha_2 t] + \exp[-2(n+1)l - z]^2/4\alpha_2 t] + 2 \exp[-2(n+1)l + z]^2/4\alpha_2 t] \right\}. \quad (50)$$

The physical interpretation of the temperature profile predicted from Eq. (50) is depicted in Fig. 4, which is typical of the Method of Images approach.²² The zero-order reflection, due to the direct diffusion of the source energy away from the front boundary, is accounted for by the term $\exp(-z^2/4\alpha_2 t)$ and the $n = 0$ term of $\exp[-(z - 2nl)^2/4\alpha_2 t]$. The odd ordered re-

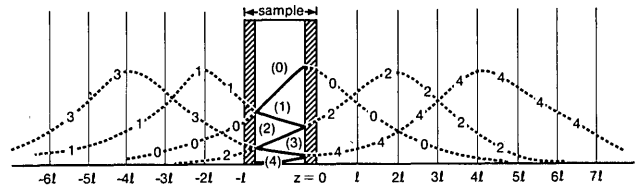


Fig. 4. Graphic depiction of Green's function solution Eq. (50) by the method of images.

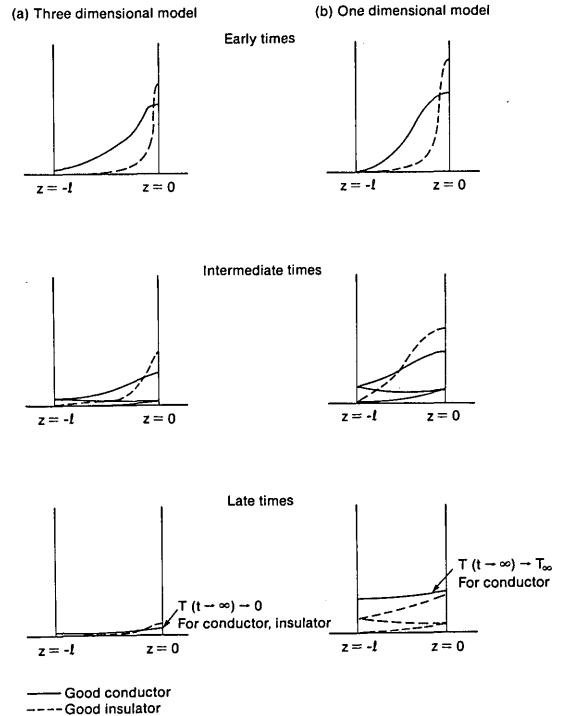


Fig. 5. Three-dimensional (a) and 1-D (b) photothermal impulse response of a sample with adiabatic boundaries at $z = 0$ and $z = -l$.

flections are accounted for by $\exp[-(z - 2nl)^2/4\alpha_2 t]$ and $\exp\{-[z - 2(n+1)l]^2/4\alpha_2 t\}$, while the even ordered reflections are accounted for by the terms of the form $\exp\{-[z + 2(n+1)l]^2/4\alpha_2 t\}$. The weighting of these terms is twice that of the other two because of the presence of the source term which doubles the value of the zero-order reflection.

The number of terms n required to bring about convergence of Eq. (50) is directly determined by the number of thermal reflections taking place at the boundaries of $z = 0$ and $z = -l$. The thermal components are reflected in a manner analogous to the reflection of acoustic waves at rigid surfaces, except that in the present case, the signals are damped with distance traveled in the medium.

The signals observed with adiabatic boundary conditions may be understood by folding or reflecting the semi-infinite response back into the region $-l \leq z \leq 0$, as shown in Figs. 4 and 5. The semi-infinite response [Eq. (25)] is a Gaussian profile in z of the form $\exp(-z^2/\sigma^2)$ with an appropriate variance $\sigma^2 = 4\alpha_2 t$. The peak value is damped over time by a factor of $1/t^{3/2}$. Consequently, the depth of penetration of the temperature

gradient in the sample is directly determined by the thermal diffusion length $\mu_s(t)$. For a given fixed time delay, the extent of thermal wave penetration into a thermally insulating sample will be relatively small, while highly conducting samples such as metals will have very long-range penetrations of the temperature profile for the same time delay.

The time evolution of the temperature profile in a sample with adiabatic boundaries is illustrated in Fig. 5. At the earliest times, for both conducting and insulating materials, the temperature profile is well approximated by the semi-infinite response of Eq. (25). At later, but still relatively early, times [Fig. 5(b)], much of the thermal energy propagating in the conductor has reached $z = -l$ and been reflected at the boundary. In the insulator, the temperature profile is still highly localized near the front surface. At relatively late times, the temperature profile in the conductor shows many reflections at $z = 0$ and $z = -l$, while in the insulator, it is damped, so that a negligible amount of energy is reflected. Similar physical trends were previously observed both experimentally and theoretically by Tam *et al.*,^{23,24} using the technique of backscattering pulsed photothermal radiometry (PTR) and 1-D mathematical analysis appropriate to excitation with large diameter laser beams.

The convergence of Eq. (50) has been addressed for a thin sample of aluminum ($\alpha_2 = 1 \times 10^{-4} \text{ m}^2/\text{s}$; $l = 20 \text{ }\mu\text{m}$). Since aluminum is a good thermal conductor, contributions to the temperature field from many reflections at $z = 0$ and $z = -l$ are required, especially at later times. It was found that all profiles converge at early times with only one term ($n = 0$) due to the dominance of the zero-order semi-infinite term. The series expansion with $n = 3$ was found to be adequate for times up to $40 \text{ }\mu\text{s}$. In the case of the aluminum sample, convergence of the series in Eq. (50) was typically obtained with $n \approx 20$ over the 0–600- μs time range. By contrast, the photothermal impulse response profiles for typical insulating solids converged after one or two terms over the same time span.

It is also possible, in the case of a sample with adiabatic boundaries, to observe a transition from the 3-D to the 1-D response as the radius of the heating beam is expanded from $w_0 \approx 0$ to $w_0 \rightarrow \infty$. This transition is examined in Fig. 6, which shows the effect of increasing the irradiation spot size w_0 from $0.1 \text{ }\mu\text{m}$ to 1 mm for a thin insulating sample ($\alpha_2 = 6 \times 10^{-8} \text{ m}^2/\text{s}$; $l = 9 \text{ }\mu\text{m}$). A 3-D \rightarrow 1-D thermal response transition is observed as the beam is expanded from a tightly focused to a defocused spot. One-dimensional heat conduction is approached as the spot size of the irradiating beam exceeds the sample thickness by a factor of ~ 2 –3. The relative spot size of the irradiating beam required to sustain 1-D heat flow is, of course, dependent on the thermal diffusivity of the sample and the attainment of the condition $w_0^2 \gg 4\alpha_2 t$. Highly conducting samples require larger beam profile sizes to achieve the 1-D heat flow.

The time profiles of the 3- and 1-D responses are inherently quite different. The only difference math-

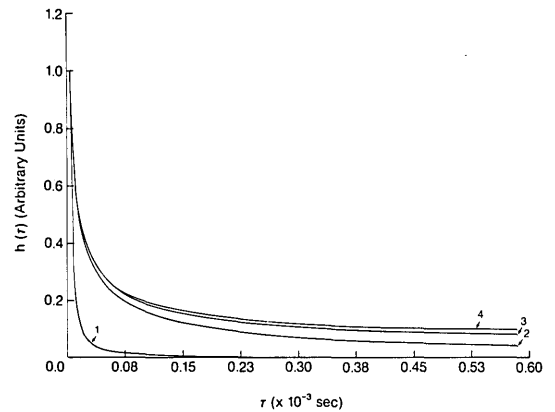


Fig. 6. Theoretical profiles of the transition from 3-D to 1-D photothermal impulse response of a 9- μm thick PVDF film ($\alpha_2 = 6 \times 10^{-8} \text{ m}^2/\text{s}$) at $r = 1 \times 10^{-7} \text{ m}$ as a function of beam waist size: $w_0 = 0.1 \text{ }\mu\text{m}$ (1), $10 \text{ }\mu\text{m}$ (2), $25 \text{ }\mu\text{m}$ (3), and $100 \text{ }\mu\text{m}$ (4).

ematically between the two cases in the present model is a shift in the time damping factor from $t^{-3/2}$ to $t^{-1/2}$ as the 1-D response is approached. This apparently minor variation in response overlies an important difference in the thermal decay channels. In the 1-D case, the only avenue for heat dissipation is longitudinal (z -direction) conduction: radial conduction does not occur. Because conduction takes place in one dimension only, the signal is damped by a factor of $t^{-1/2}$. In the 3-D case, both radial and longitudinal conduction processes contribute, which is reflected in the cubed form of the damping factor $t^{-3/2}$. The most important feature of the observed 1- and 3-D responses is the behavior at long times past excitation. The 3-D signal eventually decays to the baseline because the radial boundaries are placed at infinity [i.e., $T_2(\infty, z, t) = 0$]. The heat flux initially deposited in the sample region eventually dissipates itself over an infinite volume. In the 1-D case, the only coordinate for heat conduction is z , so that impulse energy initially deposited at $z = 0$ eventually diffuses into the sample and broadens to a uniform temperature–distance profile.²⁴ In other words, the only effect of 1-D impulse heating in a sample with adiabatic boundaries, at long times after the application of the pulse, is a spatially uniform net heating of the sample. Hence the temperature baseline attains an equilibrium value rather than going to zero. Mathematically, the later time convergence of the 1-D profile to the equilibrium, $t = \infty$, value is due to an increasing number of n values contributing as $t \rightarrow \infty$ [Eq. (50)]. The large number of n values is partially offset by the damping factor $t^{-1/2}$, which gives the uniform profile predicted as $t \rightarrow \infty$.

Because of this damping factor, the thermal decay profiles in insulators converge to much smaller equilibrium values as $t \rightarrow \infty$. These trends can be observed in Fig. 7, which compares the 1-D thermal response for a range of samples of varying α_2 at fixed l . The insulating material (bottom curve) converges to the lowest t_∞ equilibrium value of the three examples, while the highest α_2 sample achieves the equilibrium condition

much earlier than any of the other three. This trend can be understood in terms of the requirement for retention of larger quantities of energy per unit volume in insulators than in conductors in conditions of equal energy inputs, which results in lower equilibrium temperature for the insulator.

The attenuation effect of the equilibrium ($t \rightarrow \infty$) temperature in the sample's response observed for insulators may be offset by arbitrarily decreasing the sample thickness l . In very thin samples, flat equilibrium temperature/distance profile is reached sooner, because more reflections of the thermal energy may occur before time damping contributes. For the type of solid of Fig. 7 it can be shown that the effect of decreasing l on the 1-D temperature profile observed for a thermal insulator is the following: As l decreases, the temperature profile flattens at earlier times and approaches a higher equilibrium value than for thicker samples. Similar trends have been verified experimentally by Leung and Tam²³ using a short (approximate nanosecond) duration laser pulse.

C. Detection of Buried Heat Sinks

The third case of experimental interest accessed by the present theory is for a relatively thermally insulating sample layer placed in contact with a heat sink at $z = -l$ so that the boundary condition $T_2(r, -l, t) = 0$ is satisfied. The theoretical profile predicted by Eq. (40), when generalized for arbitrary z in a manner entirely similar to the method which led to Eq. (38), can be put into the following form for ease of interpretation:

$$T_2(r, z, t) = \frac{\exp(-r^2/4\alpha_2 t)}{8(\pi\alpha_2 t)^{3/2}} \left[\exp(-z^2/4\alpha_2 t) + \sum_{n=0}^{\infty} (-1)^n \left(\exp[-(2nl - z)^2/4\alpha_2 t] - \exp[-[2(n+1)l - z]^2/4\alpha_2 t] - 2 \exp[-[2(n+1)l + z]^2/4\alpha_2 t] \right) \right]. \quad (51)$$

Equation (51) yields in the limit of $z = 0$

$$\lim_{z \rightarrow 0} T_2(r, z, t) = T_2(r, 0, t) = T_1(r, 0, t); \text{ [given by Eq. (40)].}$$

The theoretical profiles predicted by Eq. (51) can be discussed in terms of Fig. 8, which examines the effect of sample thickness on the temperature time decay on placing a heat sink in contact with the lower surface at $z = -l$. The top curve is the typical 1-D semi-infinite response predicted for a sample in which the thermal profile is attenuated before much of the energy reaches $z = -l$. A heat sink placed at the rear surface of the sample has very little influence on the decay profile in this time range. As the heat sink is moved closer to the front surface, i.e., as l decreases, the temperature-time profile slopes downward until it effectively reaches the baseline at about ten multiples of the thermal transit time in the sample. For very thin samples this effect is very pronounced (bottom curve).

A similar argument applies in the case of the α_2 dependence of the response profiles. As α_2 is increased, the penetration distance of thermal waves

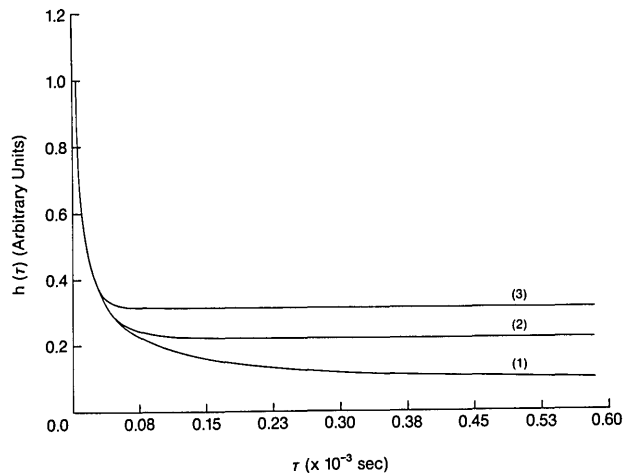


Fig. 7. Theoretical predictions of the effect of the value of sample thermal diffusivity on the decay profile of the 1-D temperature field: $\alpha_2 = 8 \times 10^{-8} \text{ m}^2/\text{s}$ (1); $4 \times 10^{-7} \text{ m}^2/\text{s}$ (2); and $8 \times 10^{-7} \text{ m}^2/\text{s}$ (3). Other parameters are $r = 1 \times 10^{-7} \text{ m}$, $l = 20 \mu\text{m}$, $w_0 = 1 \text{ mm}$; $n = 100$.

increases so that more energy reaches $z = -l$ and is attenuated by the heat sink. The effect of increasing α_2 is entirely analogous to that of decreasing l in Fig. 8. In the insulator very little energy reaches $z = -l$, and the signal decay has the familiar form of the 1-D semi-infinite profile. As the thermal diffusivity increases, more and more energy arrives at $z = -l$ causing an increasingly sharper attenuation of the response profiles after about ten thermal transit times.

VI. Summary

In this work a 3-D photothermal impulse response theory has been presented using the appropriate

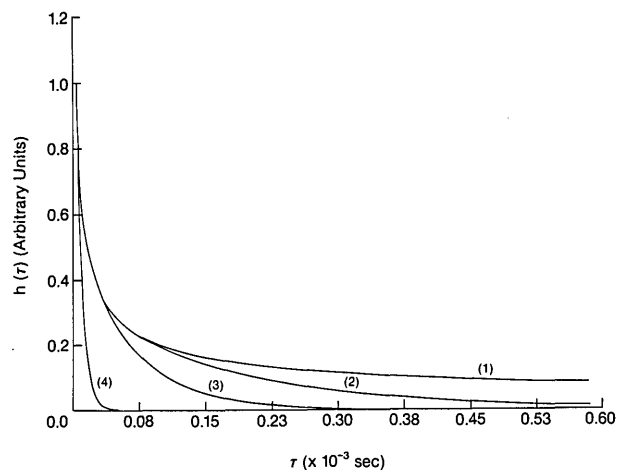


Fig. 8. One-dimensional theoretical predictions of the effect of the presence of a heat sink in contact with a solid of variable thickness: $l = 100 \mu\text{m}$ (1); $5 \mu\text{m}$ (2); $3 \mu\text{m}$ (3); and $1 \mu\text{m}$ (4). Other parameters are $r = 1 \times 10^{-7} \text{ m}$, $w_0 = 1 \text{ mm}$, $\alpha_2 = 6 \times 10^{-8} \text{ m}^2/\text{s}$; $n = 100$.

Green's function formalism with a solid of finite thickness, which is excited by a laser beam of tightly focused but finite waist size and is probed by an infinitesimally small laser probe beam in the thermorefectance configuration. Expressions have been derived for appropriate experimental geometries and the effects of system thermal, and geometric parameters on the time decay profiles of the temperature field have been discussed. Several experimental results using FM impulse response detection will be compared to our theoretical predictions in Sec. II.

Appendix A: Inversion of $\bar{I}_1(r,0,s) = \int_0^\infty \frac{J_0(kr)kdk}{\sqrt{k^2 + q_2^2}}$

\bar{I}_1 can be written in the form

$$\int_0^\infty J_0(kr) \left[\int_0^\infty \exp(-w\sqrt{k^2 + q_2^2}) dw \right] kdk,$$

so that its inverse Laplace transform

$$\begin{aligned} L^{-1}[\bar{I}_1(r,0,s)] &\equiv I_1(r,0,t) \\ &= \int_0^\infty J_0(kr) \left\{ \int_0^\infty L^{-1}[\exp(-w\sqrt{k^2 + q_2^2})] dw \right\} kdk. \end{aligned} \quad (A1)$$

Now the Laplace transform

$$L^{-1}[\exp(-w\sqrt{k^2 + q_2^2})] = \frac{w}{(4\pi\alpha_2 t)^{1/2}} \exp\left[-\left(\frac{w^2}{4\alpha_2 t} + \alpha_2 k^2 t\right)\right] \quad (A2)$$

is well-known,²⁵ so that

$$\begin{aligned} I_1(r,0,t) &= \frac{1}{(4\pi\alpha_2 t^3)^{1/2}} \int_0^\infty kdk J_0(kr) \\ &\quad \times \exp(-\alpha_2 k^2 t) \left[\int_0^\infty w \exp(-w^2/4\alpha_2 t) dw \right] \\ &= \frac{2\alpha_2 t}{(4\pi\alpha_2 t^3)^{1/2}} \int_0^\infty J_0(kr) \exp(-\alpha_2 k^2 t) kdk. \end{aligned} \quad (A3)$$

Using the result²¹ (Weber's first integral)

$$\int_0^\infty J_0(kr) \exp(-pk^2) kdk = \frac{\exp(-r^2/4p)}{2p}, \quad (A4)$$

we get

$$I_1(r,0,t) = \frac{1}{(4\pi\alpha_2 t^3)^{1/2}} \exp(-r^2/4\alpha_2 t). \quad (A5)$$

Appendix B: Inversion of $\bar{I}_G(r,0,s) =$

$$\int_0^\infty \frac{\exp(-G\sqrt{k^2 + q_2^2})}{\sqrt{k^2 + q_2^2}} J_0(kr) kdk$$

\bar{I}_G can be written

$$I_G = \int_0^\infty J_0(kr) \left[\int_0^\infty \exp[-(w+G)\sqrt{k^2 + q_2^2}] dw \right] kdk. \quad (B1)$$

Then, following the method of Appendix A, we find

$$\begin{aligned} I_G(r,0,t) &= \frac{1}{(4\pi\alpha_2 t^3)^{1/2}} \int_0^\infty J_0(kr) \exp(-\alpha_2 k^2 t) kdk \\ &\quad \times \left\{ \int_0^\infty (w+G) \exp[-(w+G)/4\alpha_2 t] dw \right\} \end{aligned}$$

or

$$I_G(r,0,t) = \frac{1}{(4\pi\alpha_2 t^3)^{1/2}} \exp(-r^2/4\alpha_2 t) \exp(-G^2/4\alpha_2 t). \quad (B2)$$

References

1. J. Opsal, A. Rosencwaig, and D. L. Willenborg, "Thermal-Wave Detection and Thin-Film Thickness Measurements with Laser Beam Deflection," *Appl. Opt.* **22**, 3169 (1983).
2. A. Mandelis, A. Williams, and E. K. M. Siu, "Photothermal Wave Imaging of Metal-Oxide-Semiconductor Field Effect Transistor Structures," *J. Appl. Phys.* **63**, 92 (1988).
3. A. Rosencwaig, J. Opsal, W. L. Smith, and D. L. Willenborg, "Detection of Thermal Waves Through Optical Reflectance," *Appl. Phys. Lett.* **46**, 1013 (1985).
4. G. L. Eesley, "Generation of Nonequilibrium Electron and Lattice Temperatures in Copper by Picosecond Laser Pulses," *Phys. Rev. B* **33**, 2144 (1986).
5. C. A. Paddock and G. L. Eesley, "Transient Thermorefectance from Thin Metal Films," *J. Appl. Phys.* **60**, 285 (1986).
6. B. M. Clemens, G. L. Eesley, and C. A. Paddock, "Time-Resolved Thermal Transport in Compositionally Modulated Metal Films," *Phys. Rev. B* **37**, 1085 (1988).
7. W. P. Leung and A. C. Tam, "Thermal Diffusivity in Thin Films Measured by Noncontact Single-Ended Pulsed-Laser-Induced Thermal Radiometry," *Opt. Lett.* **9**, 93 (1984).
8. T. Sawada and M. Kasai, "Non-Destructive Inspection of Stacking Faults and Dislocations of Semiconductor Wafers by Photoacoustic Microscopy (PAM) and Photothermal Beam Deflection (PBD)," in *Photoacoustic and Thermal Wave Phenomena in Semiconductors*, A. Mandelis, Ed. (North-Holland, New York, 1987), Chap. 1.
9. S. O. Kanstad and P.-E. Nordal, "Experimental Aspects of Photothermal Radiometry," *Can. J. Phys.* **64**, 1155 (1986).
10. A. Mandelis, "Time-Delay-Domain and Pseudorandom-Noise Photoacoustic and Photothermal Wave Processes: A Review of the State of the Art," *IEEE Trans. Ultrasonics, Ferroelectrics and Frequency Control* **UFFC-33**, 590 (1986).
11. J. F. Power and A. Mandelis, "Photopyroelectric Thin Film Instrumentation and Impulse Response Detection" (Parts I-III), *Rev. Sci. Instrum.* **58**, 2018,2024,2033 (1987).
12. M. Cardona, *Modulation Spectroscopy* (Academic, New York, 1969), pp. 117-136.
13. H. C. Chow, "Theory of Three-Dimensional Photoacoustic Effect with Solids," *J. Appl. Phys.* **51**, 4053 (1980).
14. A. Mandelis and B. S. H. Royce, "Time-Domain Photoacoustic Spectroscopy of Solids," *J. Appl. Phys.* **50**, 4330 (1979).
15. J. A. Stratton, *Electromagnetic Theory* (McGraw-Hill, New York, 1941), p. 573; A. Sommerfeld, *Ann. Phys.* **28**, 665 (1909).
16. A. Rosencwaig and J. Opsal, "Thermal Wave Imaging with Thermoacoustic Detection," *IEEE Trans. Ultrasonics, Ferroelectrics and Frequency Control* **UFFC-33**, 516 (1986).
17. R. Bellman, R. E. Marshak, and G. M. Wing, "Laplace Transform Solution of Two-Medium Neutron Aging Problem," *Philos. Mag.* **40**, 297 (1949).
18. H. S. Carslaw and J. C. Jaeger, *Conduction of Heat in Solids* (Oxford U.P., London, 1959), Chap. 14.
19. Ref. 18, Chap. 10.10.V.
20. Ref. 18, Chap. 10.3.
21. G. N. Watson, *A Treatise on the Theory of Bessel Functions* (Cambridge U.P., London, 1944), p. 393.

22. P. M. Morse and H. Feshbach, *Methods of Theoretical Physics* (McGraw-Hill, New York, 1953), p. 812.
23. W. P. Leung and A. C. Tam, "Techniques of Flash Radiometry," *J. Appl. Phys.* **56**, 153 (1984).
24. A. C. Tam, "Pulsed Laser Photoacoustic and Photothermal Detection," in *Photoacoustic and Thermal Wave Phenomena*

in *Semiconductors*, A. Mandelis, Ed. (North-Holland, New York, 1987), Chap. 8.

25. M. Abramowitz and I. A. Stegun, Eds., *Handbook of Mathematical Functions* (National Bureau of Standards, Washington, DC, 1964), p. 229.

Whipple continued from page 3340

expands and contracts, the precisely fashioned figure changes shape and degrades the image at focus. The traditional solution to this problem has been to make the mirror out of the most thermally inert substance possible. (The 6-m mirror, currently the world's largest, is made from a special low-expansion glass.) Various ceramics, specialized kinds of glass, and natural and man-made quartz have all been used. But all these materials are quite expensive and difficult to work with.

A telescope mirror that is not at the same temperature as the surrounding air causes another problem. As the typically warmer mirror releases heat into the cooler surrounding air, the air immediately above the mirror's surface becomes warmer than ambient air and disturbs the incoming starlight.² The low mass and open structure of the spun-cast mirrors should enable them to remain close in temperature to that of the ambient air and thereby minimize the above problems. The possibility of controlling a mirror's temperature by, in one scheme, blowing temperature-controlled air through its core is being explored.

As a prelude to measuring the 48-in. mirror's thermal performance, the University of Arizona's Optical Sciences Center is grinding and polishing the blank to a spherical curve to allow optical testing. Once this initial figure is achieved, the mirror will be heated and cooled, cycling it between 32° and 68°F. The quality of image produced by the mirror will be tested at different temperatures during the cycles to determine how well the mirror maintains its figure.

After testing concludes, the observatory will go out on bid for a contractor to polish the mirror to its final figure. After polishing, the honeycomb mirror will weigh 310 pounds. The 48-in. telescope will be of the Ritchey-Chrétien optical design. This means that both the primary and secondary mirrors will have a hyperbolic shape rather than the more usual spherical or parabolic curvature. While the hyperbolic shapes are more difficult to polish into the finished optics, the resulting telescope will have good quality images over a far wider field of view.

The main disadvantage of a parabolic reflector, such as the present 24-in. mirror, is its very small field of good focus. The 200-in. Hale Reflector on Palomar Mountain, for example, gives its best image quality over an area only one-fifteenth of the moon's diameter. In contrast, the 48-in. reflector will have good imaging over the complete diameter of the full moon.

The 48-in. telescope will have a chopping secondary mirror for infrared astronomy. Infrared astronomers need to measure constantly the overall infrared emission from the background sky as they observe. The sky background is then subtracted to determine the actual infrared radiation of an object. This differential measurement can be accomplished by having the telescope's secondary mirror tilt or chop from its normal position so that the astronomer can measure the infrared radiation from the vacant sky next to the object of study. The mirror then flips back to its normal position to

restore the astronomical object to view. The 48-in. telescope's secondary mirror will chop five times per second.

Instrument specialists at Smithsonian Astrophysical Observatory headquarters in Cambridge, MA, are completing a 2-D infrared array for the telescope. This recent development in detector technology "will allow routine infrared imaging for the first time at the observatory," resident astronomer Nelson Caldwell says.

Before the infrared arrays, infrared detectors were usually single-element devices that could measure the strength of an infrared radiation source but could not provide a picture of the object. The instrument specialists also plan to develop a large-format charge-coupled-device camera for the telescope. CCD cameras replace film with electronic light-measuring elements. Images of stars and galaxies are recorded as digital information stored on magnetic tape for later computer analysis. The new camera could have a detector area as much as 16 times larger than that of the CCD currently in use on the 24-in. telescope. A new computer, already on site, will control the detector packages on the new telescope and handle the data. To reduce costs, the existing 24-in. telescope's dome and part of the telescope mount will be used by the 48-in. instrument.

With the astronomy community planning the construction of telescopes many times larger than the 48-in. reflector, why build such a relatively small instrument? One reason is that not all astronomical research requires large telescopes. Astronomers request time on telescopes appropriate to their research projects. Very large telescopes are reserved for studying the faintest objects, which require enormous light-collecting power. Also, the 48-in. reflector, with its new ultrasensitive light-detector packages, can be used for research that would have required a much larger telescope a generation ago.

Telescope-time-allocation committees at observatories typically have two or more requests for each night of telescope time available. David Latham, associate director of the Center for Astrophysics' Optical and Infrared Division, says he expects the 48-in. reflector to fall into this oversubscribed category. "A 48-inch telescope with a new computer and the latest in detector packages will be a formidable addition to our research capability at Whipple Observatory," Latham says.

1. At Research Reports press time, a 3.5-meter-diameter mirror was slowly cooling as it was being annealed in the University of Arizona's spinning furnace. On 21 April, 45,000 pounds of glass were loaded into the mold. The furnace was fired on 23 April, and the mirror was spun at eight revolutions per minute 25 and 26 April. The annealing process started 28 April. During this process, the temperature is being lowered one-half degree per hour until the mirror reaches room temperature. The mirror, destined for a telescope in New Mexico, should be removed from the furnace at the end of May.
2. Light's direction of travel changes as it changes medium. A common example is seen over an asphalt road on a hot day in the form of a "wavy" effect, caused by light rays being bent as they traverse layers of air at different temperatures.